THE UNIVERSITY of EDINBURGH

Edinburgh Research Explorer

From the paddle to the beach - A Boussinesq shallow water numerical wave tank based on Madsen and Sorensen's equations

OPEN ACCESS

From the paddle to the beach - a Boussinesq shallow water numerical wave tank based on Madsen and Sørensen's equations

Jana Orszaghova [a,*], Alistair G.L. Borthwick[a], Paul H. Taylor[a]

[a]*Department of Engineering Science, University of Oxford, Parks Road, Oxford, OX1 3PJ, UK*

Abstract

This article describes a one-dimensional numerical model of a shallow-water flume with an in-built piston paddle moving boundary wavemaker. The model is based on a set of enhanced Boussinesq equations and the nonlinear shallow water equations. Wave breaking is described approximately, by locally switching to the nonlinear shallow water equations when a critical wave steepness is reached. The moving shoreline is calculated as part of the solution. The piston paddle wavemaker operates on a movable grid, which is Lagrangian on the paddle face and Eulerian away from the paddle. The governing equations are, however, evolved on a fixed mapped grid, and the newly calculated solution is transformed back onto the moving grid via a domain mapping technique. Validation test results are compared against analytical solutions, confirming correct discretisation of the governing equations, wave generation via the numerical paddle, and movement of the wet/dry front. Simulations are presented that reproduce laboratory experiments of wave runup on a plane beach and wave overtopping of a laboratory seawall, involving solitary waves and compact wave groups. In practice, the numerical model is suitable for simulating the propagation of weakly dispersive waves and can additionally model any associated inundation, overtopping or inland flooding within the same simulation.

Keywords: Boussinesq, wave propagation, runup, overtopping, piston paddle

Contents

*jana.orszaghova@eng.ox.ac.uk

1. Introduction

Numerical models based on Boussinesq-type equations are increasingly popular operational predictive tools in coastal engineering. These essentially two dimensional models avoid free surface boundary issues by explicitly eliminating the vertical coordinate, yet retaining some vertical flow structure. Nowadays Boussinesq-type models are being applied to relatively large scale coastal problems (see for example Fuhrman and Madsen (2009), Lynett et al. (2010)). It should be noted that there are other approaches used in practice based on non-hydrostatic shallow flow solvers (see Stansby and Zhou (1998), Zijlema and Stelling (2008)).

The classical Boussinesq equations derived by Peregrine (1967) were limited to weakly nonlinear and weakly dispersive waves and assumed $O(\varepsilon) = O(\mu^2)$, whereby nonlinearity ε represents the ratio of wave amplitude to depth, and dispersion μ is the ratio of depth to wavelength. Since 1967, there have been considerable attempts at extending the applicability of Boussinesq equations both onshore and offshore. Comprehensive reviews of the earlier development of the field, including derivations, can be found in Dingemans (1997) and Madsen and Schäffer (1999). Of the myriads of candidates, the enhanced equation set by Madsen and Sørensen (1992) is $O(\varepsilon, \mu^2)$ accurate, yet has improved dispersion properties thanks to a mathematical manipulation of the dispersive terms. The incorporation of a Padé approximant of the linear dispersion relation into the momentum equations, as suggested by Madsen and Sørensen (1992), results in equations suitable for water depth as deep as $\mu = 0.5$ (approximately equivalent to $kh = 3$, with k representing the wavenumber and h is the still water depth). The vertical profile in this extended deeper region is not properly modelled, due to the underlying assumption of the quadratic vertical variation of the horizontal velocity, yet the wave propagation in the extended region is captured with reasonable

accuracy. Another widely used equation set was derived by Nwogu (1993), and possesses equivalent dispersion properties. Nwogu's equations are formulated in terms of the surface elevation and horizontal velocity at a specific depth chosen to minimise wave propagation errors from linear theory. Further extensions to the validity of Boussinesq-type equations have been achieved by deriving fully nonlinear equations, whereby $O(\varepsilon) = 1$ is assumed, as well as deriving higher order equations which retain $O(\mu^4)$ and equivalent terms (see for example Wei et al. (1995), Gobbi et al. (2000), Agnon et al. (1999), Madsen et al. (2003)). The emphasis in much of this work is to extend the range of applicability of Boussinesq models into deeper water. In contrast, the present paper seeks to extend the applicability of a simple Boussinesq model to zero depth.

Boussinesq-type equations cannot model wave breaking, unless they are modified to account for the associated energy dissipation. The most common breaking treatments in the Boussinesq framework are the surface roller concept (see Schäffer et al. (1993)) or the inclusion of artificial viscosity in the momentum equation (see Zelt (1991), Karambas and Koutitas (1992)). These have been successful and facilitated the application of solvers to regions further inshore into the surf zone, but at the cost of requiring tunable parameters. On the other hand, the nonlinear shallow water equations are appropriate for modelling broken waves in the surf zone. Dissipation of energy is captured physically correctly (see textbooks on shallow water shock conditions, for example Section 2.7 in Johnson (1997)). Due to the lack of frequency dispersion in the nonlinear shallow water equations, any waveform modelled by these equations has a tendency to shock up to produce bores or hydraulic jumps, even on a horizontal bottom. For this reason the equations cannot be used pre-breaking, as they would lead to incorrect and premature breaking.

The present paper describes a hybrid numerical model based on the Boussinesq equations derived by Madsen and Sørensen (1992) pre-breaking and the nonlinear shallow water equations post-breaking. In this way the appropriate governing equations are applied at all stages as the wave propagates from intermediate to shallow water. Our hybrid model builds upon work of Borthwick et al. (2006). Recently there have been similar hybrid models proposed by Tonelli and Petti (2009) and Bonneton et al. (2011). Although the chosen set of Boussinesq equations contains less of the physics and is relatively unsophisticated compared to the newer derivations (see above), it has been selected for its simplicity (small number of low order terms) and relative ease for numerical computation. In our model, the breaking criterion, which triggers a local switch from Boussinesq to the nonlinear shallow water equations, is based on local wave steepness. An appropriate shock capturing numerical scheme is applied to the nonlinear shallow water equations in order to capture the propagating bores. A well-established Godunov-type finite volume method, with data reconstruction, is used, following Hu et al. (2000), Hubbard and Dodd (2002), Liang and Borthwick (2009) among others. Such methods additionally allow for natural treatment of the moving shoreline. This is computed as part of the solution, so there is no need for any tracking of the wet/dry front. The model can thus deal with multiple shorelines and splitting of the water mass, as can occur during an overtopping event. The Boussinesq equations are solved using finite differences, as smooth solutions are expected pre-breaking.

A novel feature of the present numerical model is the inclusion of a full model for a

piston paddle wavemaker. It allows for complete simulations of shallow water laboratory experiments, including the wave generation process. The problem of the time-varying domain size, due to the paddle movement, is overcome by implementing a domain transformation, so that calculations are performed in a fixed domain. This horizontal transformation bears resemblance to a σ-transformation used in the vertical coordinate in three-dimensional free surface flow problems (as an example see Turnbull et al. (2003)).

The paper is structured as follows. Section 2 outlines the governing equations of the hybrid model and how the piston paddle is modelled as a moving boundary. The treatment of wave breaking is also discussed. Section 3 describes the numerical methods used to solve the governing equations, the wetting and drying algorithm, and the boundary conditions. Special attention is given to the moving grid adjacent to the paddle. The model is validated against analytical solutions and experimental measurements in Sections 4 and 5. In Section 4.1 an exact numerical solution for solitary waves in the present Boussinesq equations is derived, together with the relation between the solitary wave amplitude and celerity.

2. Governing equations

The hybrid model uses two sets of governing equations. The enhanced Boussinesq equations derived by Madsen and Sørensen (1992) are used pre-breaking and the nonlinear shallow water equations post-breaking. A stage-discharge (η, q) formulation is adopted for both equation sets, where η denotes the water surface level above a prescribed horizontal datum and q denotes the depth-integrated horizontal flux. Figure 1 illustrates the free surface flow problem along with the relevant variables. The (η, q) formulation correctly balances the flux gradient and source terms in the shallow water momentum equation when discretized within a Godunov-type finite volume framework and is particularly well suited to simulations involving wetting and drying (see Liang and Borthwick (2009)). The resulting equation set is appropriate for modelling wave runup, overtopping and coastal flooding scenarios. The Boussinesq equations are also expressed in terms of (η, q) to facilitate joining of the two equation sets in the present model.
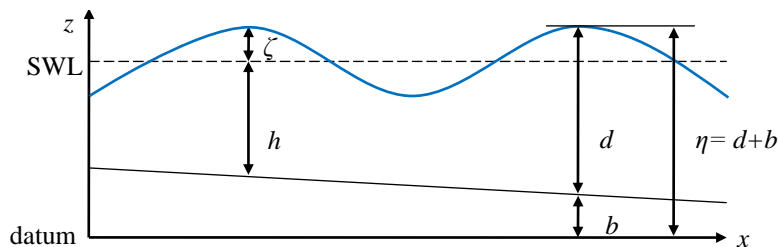

Figure 1: Definition sketch.

2.1. Nonlinear shallow water equations

The nonlinear shallow water equations are a non-dispersive depth-averaged approximation of the three dimensional water wave problem. Written in the usual depth-discharge

4

(d, q) formulation, for one horizontal dimension, the equations are

$$\zeta_t + q_x = 0 \tag{1}$$

and

$$q_t + \left(\frac{q^2}{d}\right)_x + gd\zeta_x + \frac{\tau_b}{\rho} = 0, \tag{2}$$

where the subscripts t and x denote partial derivatives with respect to time and space, g is the magnitude of gravitational acceleration, ρ is the water density and τ_b is the bottom friction, given empirically by

$$\tau_b = \rho C_f u |u|, \tag{3}$$

where C_f denotes the friction coefficient. By using $gd\zeta_x = g(\eta - b)\eta_x = \frac{1}{2}g(\eta^2 - 2\eta b)_x + g\eta b_x$, where b is the bed elevation above the horizontal datum and $d_t = \eta_t$ for a fixed bed, (see Liang and Borthwick (2009)), the nonlinear shallow water equations become

$$\eta_t + q_x = 0 \tag{4}$$

and

$$q_t + \left(\frac{q^2}{d} + \frac{1}{2}g(\eta^2 - 2\eta b)\right)_x = -\frac{\tau_b}{\rho} - g\eta b_x. \tag{5}$$

Equations (4) and (5) form a hyperbolic set of equations $\boldsymbol{q}_t + \boldsymbol{f}(\boldsymbol{q})_x = \boldsymbol{s}$, with $\boldsymbol{q}$ representing the vector of conserved variables (η, q), $\boldsymbol{f}$ the vector of fluxes, and $\boldsymbol{s}$ the source terms.

2.2. Boussinesq equations

The enhanced Boussinesq equations by Madsen and Sørensen (1992) retain first orders of nonlinearity and dispersion, and as such contain additional dispersive terms in the momentum equation compared to the nonlinear shallow water equations (4) and (5). The Boussinesq set expressed in terms of (η, q) is

$$\eta_t + q_x = 0 \tag{6}$$

and

$$q_t + \left(\frac{q^2}{d} + \frac{1}{2}g(\eta^2 - 2\eta b)\right)_x = -\frac{\tau_b}{\rho} - g\eta b_x + \left(B + \frac{1}{3}\right)h^2 q_{xxt} + Bgh^3\eta_{xxx} +$$
$$+ hh_x\left(\frac{1}{3}q_{xt} + 2Bgh\eta_{xx}\right), \tag{7}$$

where B represents the Boussinesq linear dispersion coefficient. Setting $B = \frac{1}{15}$ embeds the [2][2] Padé approximant of the linear dispersion relation into the momentum equation. Setting $B = 0$ reverts back to the classical Boussinesq equations originally derived by Peregrine (1967).

Note that the presence of h, the still water depth, in equation (7) is acceptable since the Boussinesq equations are applied in parts of the domain where h and ζ are well defined, as shall be discussed in more detail in Section 2.4.

In order to facilitate Runge-Kutta time-stepping, the momentum equation is recast in the same way as suggested by Bradford and Sanders (2001) and becomes

$$q_t^* = -\left(\frac{q^2}{d} + \frac{1}{2}g(\eta^2 - 2\eta b)\right)_x - \frac{\tau_b}{\rho} - g\eta b_x + Bgh^3\eta_{xxx} + 2Bgh^2 h_x \eta_{xx}, \tag{8}$$

where

$$q_t^* = q_t - \left(B + \frac{1}{3}\right)h^2(q_t)_{xx} - \frac{1}{3}hh_x(q_t)_x. \tag{9}$$

2.3. Piston paddle and wave generation

In shallow water laboratory flumes, piston paddles are often used for wave generation. The paddle moves back and forth according to the supplied paddle signal. Following Hughes (1993), the paddle velocity is equal to the local depth-averaged particle velocity of the generated wave. Therefore to find the paddle displacement time series $x_p(t)$, one needs to solve

$$\frac{dx_p}{dt} = \overline{u}(x_p, t), \tag{10}$$

where $\overline{u} = \frac{q}{d}$ is the depth-averaged particle velocity. For a large paddle sweep, such as occurs when generating solitary waves, equation (10) has to be solved for x_p. For relatively small paddle sweeps, the paddle displacement signal is simply calculated from

$$\frac{dx_p}{dt} = \overline{u}(0, t), \tag{11}$$

assuming the initial paddle position is at $x = 0$.

While the paddle operates, the size of the domain changes. The effective length of the tank reduces as the paddle moves forwards to create a wave crest. Similarly, the domain lengthens when the paddle moves backwards to create a wave trough. In order to incorporate this, we use a mathematical transformation T, which maps the time-varying physical domain in the vicinity of the paddle, referred to as the *paddle domain*, onto a fixed computational domain. Although the transformed governing equations contain time-varying parameters, these pose minimal additional difficulty for the numerical solver. As shown in Figure 2, the *paddle domain* is defined by $x \in [x_p(t)\ m_0]$ with m_0 representing the location of the end of the *paddle domain*. The length of the *paddle domain* is given by $m(t) = m_0 - x_p(t)$. The value of m_0 is calculated at the beginning of each simulation, and is set to be, to the nearest grid point, 10 times the maximum paddle sweep.
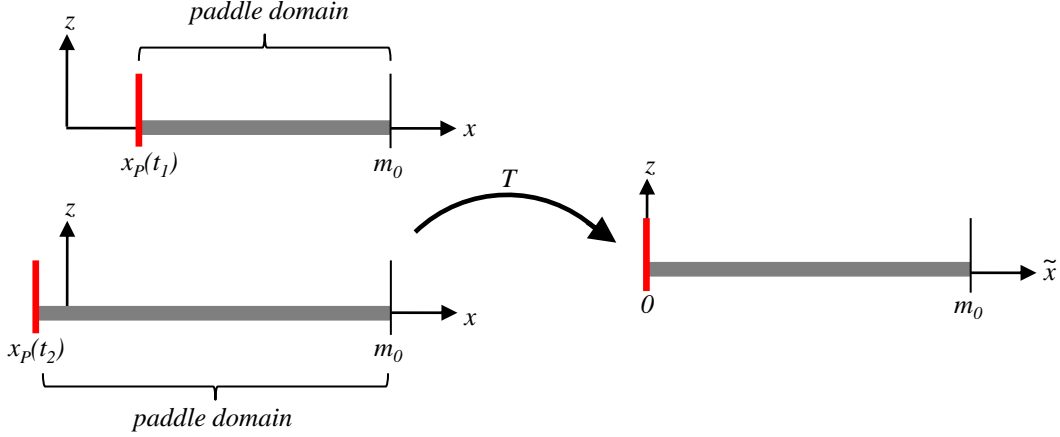
Figure 2: Transformation sketch.

By applying the transformation T of the independent variable x, such that

$$T(x) = \tilde{x} = \frac{m_0}{m(t)}\big(x - x_p(t)\big), \tag{12}$$

the time-varying *paddle domain* is mapped onto a fixed $\tilde{x} \in [0 \; m_0]$ domain with the mapped governing equations being

$$\eta_t = -\frac{1}{m}m_t(m_0 - \tilde{x})\eta_{\tilde{x}} - \frac{m_0}{m}q_{\tilde{x}} \tag{13}$$

and

$$
\begin{aligned}
q_t^{**} ={}& -\frac{1}{m}m_t(m_0 - \tilde{x})q_{\tilde{x}} - \frac{m_0}{m}\Big(\frac{q^2}{d} + \frac{1}{2}g(\eta^2 - 2\eta b)\Big)_{\tilde{x}} - \frac{\tau_b}{\rho} - g\eta\frac{m_0}{m}b_{\tilde{x}} \\
&+ \Big(B + \frac{1}{3}\Big)h^2\Big(\frac{m_0}{m}\Big)^2\frac{1}{m}m_t\big((m_0 - \tilde{x})q_{\tilde{x}\tilde{x}\tilde{x}} - 2q_{\tilde{x}\tilde{x}}\big) + Bgh^3\Big(\frac{m_0}{m}\Big)^3\eta_{\tilde{x}\tilde{x}\tilde{x}} \\
&+ 2Bgh^2h_{\tilde{x}}\Big(\frac{m_0}{m}\Big)^3\eta_{\tilde{x}\tilde{x}} + \frac{1}{3}hh_{\tilde{x}}\Big(\frac{m_0}{m}\Big)^2\frac{1}{m}m_t\big((m_0 - \tilde{x})q_{\tilde{x}\tilde{x}} - q_{\tilde{x}}\big),
\end{aligned}
\tag{14}
$$

where

$$q_t^{**} = q_t - \Big(B + \frac{1}{3}\Big)h^2\Big(\frac{m_0}{m}\Big)^2(q_t)_{\tilde{x}\tilde{x}} - \frac{1}{3}hh_{\tilde{x}}\Big(\frac{m_0}{m}\Big)^2(q_t)_{\tilde{x}}. \tag{15}$$

2.4. Switch between the equation sets and treatment of wave breaking

The hybrid numerical model is suitable for non-breaking and breaking waves. The Boussinesq equations (13),(14) with (15) and (6),(7) with (9) are solved for smooth and non-breaking waves. Once the waves break, they are modelled as bores by the nonlinear shallow water equations (4) and (5). An ad-hoc breaking initiation criterion is based on the local free surface slope η_x. At the beginning of every time step, the domain is separated into individual waves using a down-crossing method. The maximum wave steepness η_x is calculated for every wave. The most offshore wave with $|\eta_x| \geq 0.4$ determines the current

7

breaking location. Remarkably, this single value of the breaking wave slope works well for all the test cases we have modelled, both solitary waves and steep dispersive wave groups. The switch from the Boussinesq equations to the nonlinear shallow water equations is shifted a quarter of a wavelength offshore from the location of the maximum wave steepness. Switching between the two equations sets is a matter of retaining or neglecting the dispersive terms since the shallow water equations are a subset of the Boussinesq equations. Also, to minimize any instabilities in the flow, the dispersive terms are ramped down smoothly over half a wavelength. The breaking location, if it exists, is then recalculated at the next time step so that the breaking region follows the wave inshore, and at the original breaking location Boussinesq equations can be re-established. In practice, this very simple treatment of wave breaking does not require any additional calibration and re-tuning for simulations reproducing laboratory-scale waves. A similar concept has also been used by Borthwick et al. (2006), Tonelli and Petti (2009) and Bonneton et al. (2011), with the breaking initiation criterion dependent on the vertical velocity component of the free surface, the wave nonlinearity $\varepsilon = \frac{\zeta}{h}$ and the local energy dissipation respectively.

Additionally, the shallowness parameter $\mu = \frac{h}{\lambda}$, with λ representing a typical wavelength, is also considered. The shallow water equations are solved in all sections of the domain where $\mu \leq \frac{1}{20}$ and dispersive effects are negligible. This is mathematically consistent as the shallow water equations are essentially a non-dispersive approximation of the Boussinesq equations. Bellotti and Brocchini (2002) demonstrate that dispersive $O(\mu^2)$ terms diminish close to the shoreline, unlike dispersive-nonlinear terms such as $O(\varepsilon\mu^2)$. However, since the Boussinesq equations of Madsen and Sørensen (1992) are of $O(\varepsilon, \mu^2)$ accuracy, the problem identified by Bellotti and Brocchini (2002) does not apply to the present hybrid model.

3. Numerical implementation

3.1. Computational grids for the Boussinesq equations

Let the physical domain under consideration be defined as $x \in [0\ L]$, where L denotes the length of the flume. Initially, the paddle is at rest such that $x_p(0) = 0$. The initial underlying uniform computational grid x_i^0 is defined by

$$x_i^0 = (i-1)\Delta x, \text{ where } \Delta x = \frac{L}{(M-1)}, \qquad \text{for } i = 1 \ldots M, \tag{16}$$

where M is the total number of grid points and Δx is the spacing between any two adjacent grid points x_i^0.

However, as discussed in Section 2.3, the size of the domain changes according to the paddle movement. For this reason, the *paddle domain* $x \in [x_p\ m_0]$ is mapped onto a fixed $\tilde{x} \in [0\ m_0]$ domain. The value of m_0, which defines the end of the *paddle domain*, is given by

$$m_0 = (\widetilde{M} - 1)\Delta x, \text{ where } (\widetilde{M} - 1) \text{ is the nearest integer of } \max_t \frac{10x_p(t)}{\Delta x}. \tag{17}$$

In the transformed *paddle domain* $\tilde{x} \in [0 \; m_0]$, a uniform computational grid $\tilde{x}_i$ is used, such that

$$\tilde{x}_i = (i-1)\Delta\tilde{x}, \text{ where } \Delta\tilde{x} = \frac{m_0}{(\widetilde{M}-1)} = \Delta x, \qquad \text{for } i = 1\ldots\widetilde{M}, \tag{18}$$

where $\widetilde{M}$ is the number of grid points in the transformed *paddle domain* and $\Delta\tilde{x} = \Delta x$ is the spacing between any two adjacent grid points $\tilde{x}_i$ in the transformed domain. The solution is calculated in the fixed transformed domain $\tilde{x} \in [0 \; m_0]$. It is then mapped onto the physical domain using the inverse transformation T^{-1}, which follows from (12). The solution grid of the original time-varying *paddle domain* $x \in [x_p \; m_0]$ is also recovered using T^{-1} such that

$$x_i = x_p + \frac{m}{m_0}(i-1)\Delta x \qquad \text{for } i = 1\ldots\widetilde{M}. \tag{19}$$

It is clear that this solution grid varies in time since $m = m(t)$ and $x_p = x_p(t)$. Spacing between any two grid points x_i is given by $\frac{m}{m_0}\Delta x$, which is a function of time. When the paddle moves forwards such that $x_p > 0$, the *paddle domain* contracts and the grid spacing between individual grids points x_i decreases, since under these circumstances $m < m_0$ and therefore $\frac{m}{m_0}\Delta x < \Delta x$. Equivalently, when the paddle moves backwards such that $x_p < 0$, the *paddle domain* expands and the spacing increases, since in this case $m > m_0$ and therefore $\frac{m}{m_0}\Delta x > \Delta x$. Figure 3 shows the adapting solution grid with $m_0 = 1$ m.
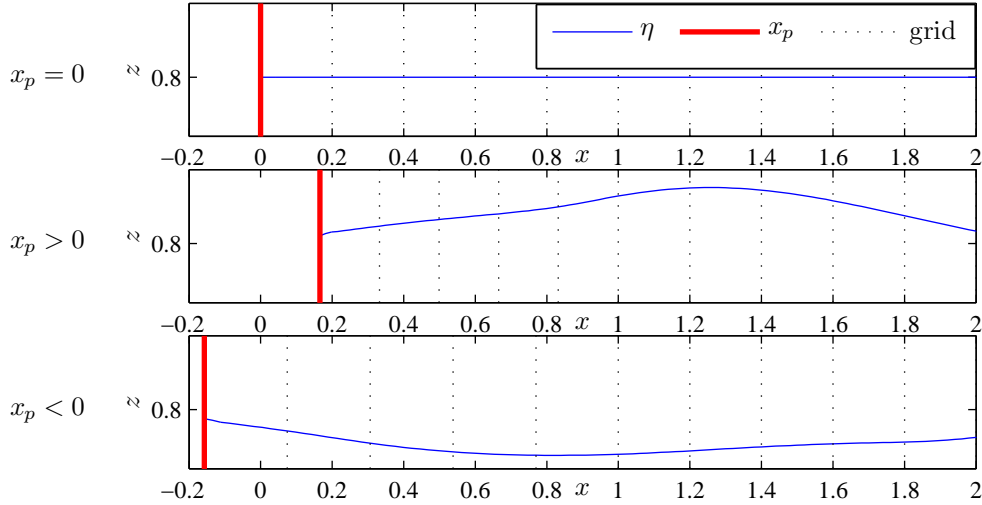

Figure 3: Adapting solution grid in the *paddle domain* for $x \le 1$ m. Fixed computational grid for $x > 1$ m.

The Eulerian region of the domain, where the untransformed Boussinesq equations (6), (8) and (9) are solved, utilizes a uniform grid

$$x_i = (i-1)\Delta x \qquad \text{for } i = \widetilde{M}+1\ldots M_{switch}, \tag{20}$$

where M_{switch} is the index of the last grid point solved by the Boussinesq equations. As discussed in Section 2.4, the switch between the Boussinesq equations and the shallow water

9

equations is determined at every time step according to the local wave steepness η_x and the dispersion parameter μ; therefore, $M_{switch} = M_{switch}(t)$. Figure 3 shows part of the fixed uniform grid for $x > 1$ m.

3.2. Finite difference discretisation for the Boussinesq equations

Both Boussinesq equation sets (6), (8) with (9) and (13), (14) with (15) are discretized and solved using finite differences. Spatial derivatives are approximated by 5-point centered stencils leading to overall second order accuracy. As pointed out by Wei and Kirby (1995), this ensures that the truncation error arising from approximating first order derivatives is smaller than the third order derivative dispersive terms in the momentum equations (8) and (14).

When discretising, care has to be taken at the interface between the *paddle domain* and the rest of the Boussinesq domain, as different governing equations and computational grids are used on either side of the grid point $\widetilde{M}$. Therefore, when approximating spatial derivatives with respect to $\tilde{x}$ at grid points $\widetilde{M}-1$ and $\widetilde{M}$; and spatial derivatives with respect to x at grid point $\widetilde{M}+1$, standard discretisation formulae have to be adapted to account for the non-uniform grid spacing. For reference, the first derivative approximation for an arbitrary function f at grid point $\widetilde{M}-1$ is shown in (21), where $f_i = f(\tilde{x}_i)$. Equivalent expressions for grid points $\widetilde{M}$ and $\widetilde{M}+1$, and for higher derivatives have been omitted for brevity.

$$
\begin{aligned}
f_{\tilde{x}}(\tilde{x}_{\widetilde{M}-1}) &\approx \frac{1}{\Delta x}\left(\frac{m+m_0}{6(3m+m_0)}\right)f_{\widetilde{M}-3} - \frac{1}{\Delta x}\left(\frac{m+m_0}{2m+m_0}\right)f_{\widetilde{M}-2} - \frac{1}{\Delta x}\left(\frac{m-m_0}{2(m+m_0)}\right)f_{\widetilde{M}-1} \\
&+ \frac{1}{\Delta x}\left(\frac{m+m_0}{3m_0}\right)f_{\widetilde{M}} - \frac{1}{\Delta x}\left(\frac{2m^4}{m_0(m+m_0)(2m+m_0)(3m+m_0)}\right)f_{\widetilde{M}+1}. \quad (21)
\end{aligned}
$$

The Boussinesq equations (6), (8) and (13), (14) are integrated forward in time using a fourth order Runge-Kutta method for a system of equations (see page 303 of Spencer et al. (1977)). At each of the 4 intermediate steps, equations (9) and (15) have to be solved for q_t, in order to be able to update the intermediate rates of change of η and q, usually denoted by $k_{r1}, \ldots, k_{r4}$ with $r = 1$ for η and $r = 2$ for q. Discretized equations (9) and (15) form a pentadiagonal system of equations, which is efficiently solved by a simple extension of the Thomas algorithm. An initial value for a time step Δt is input into the model at the beginning of a simulation. At each time level, the Courant-Friedrichs-Lewy condition is checked and, if need be, the time step Δt is reduced so that

$$
\Delta t \leq \Delta t_{CFL} = C \min_i \frac{\Delta x}{|u_i| + \sqrt{gd_i}}, \quad (22)
$$

where C is the Courant number, $u_i = \frac{q_i}{d_i}$ is the depth-averaged horizontal velocity and d_i the total water depth at the ith grid point. For all calculations performed in this paper $0.8 \leq C \leq 1$ was used.

In order to avoid undesirable oscillations, the dispersive terms in (14) and (15) are neglected at the first two grid points closest to the paddle. Over such a short distance, lack

of dispersion is assumed insignificant. Boundary conditions at the paddle are calculated as part of the solution utilizing the known paddle displacement signal. The updated value of η on the paddle, denoted by η_1^{n+1}, is calculated as described above, but using forward stencils for discretization of spatial derivatives. The updated value of q at the paddle, denoted by q_1^{n+1}, is calculated from $q_1^{n+1} = (\eta_1^{n+1} - b_1)u_p$, where b_1 is the bed elevation at the paddle and $u_p(t)$ is the paddle velocity calculated from the supplied paddle displacement signal by differentiating x_p with respect to t. Numerical tests using fictitious grid points as well as Riemann invariants have been carried out for calculating the updated solution values at the paddle. However, the use of forward stencils gave the most stable results, and therefore has been implemented in the numerical model.

When the paddle comes to rest at the end of the paddle displacement signal, it acts as a fully reflective solid boundary. The free surface elevation at the paddle η_1^{n+1} is calculated as part of the solution utilizing fictitious grid points. At the fictitious grid points, η and q are defined using known values as

$$\eta_0^n = \eta_2^n, \ q_0^n = -q_2^n \quad \text{and} \quad \eta_{-1}^n = \eta_3^n, \ q_{-1}^n = -q_3^n. \tag{23}$$

Since there can be no flow through the stationary paddle, the flux is given by $q_1^{n+1} = 0$. In simulations where the whole domain is solved by the Boussinesq equations, identical treatment of the solid right-hand side boundary is carried out.

3.3. Finite volume scheme for the nonlinear shallow water equations

The integral form of the nonlinear shallow water equations (4) and (5) is solved by a Godunov-type finite volume scheme on a uniform grid x_i such that

$$x_i = (i-1)\Delta x \qquad \text{for } i = M_{switch} + 1 \dots M, \tag{24}$$

where x_i denotes the centre of the ith grid cell with width of Δx. Following Liang and Borthwick (2009), the intercell fluxes are calculated with the HLL approximate Riemann solver, which has been extended for dry bed scenarios (see Fraccarollo and Toro (1995)). Slope-limited data reconstruction and two-step predictor-corrector time-stepping of the MUSCL-Hancock method lead to second order accuracy in time and space of the numerical scheme. A minmod slope limiter is used used in all computations.

Wetting and drying at the moving shoreline is calculated as part of the solution. We adopt the approach devised by Brufau et al. (2002) whereby local bed modification at the wet-dry front ensures correct flow features. Dry cells are excluded from the computational domain unless they are about to be flooded. Figure 4 depicts two possible scenarios at a left-hand side wet-dry front. When the water level of the left wet cell is below or the same as the bed level of the right dry cell, $\eta_L \leq \eta_R = b_R$, temporarily setting $b_R = \eta_L$ and $q_R = -q_L$ ensures no flow between the two cells, as desired. Alternatively, when the water level of the left wet cell is above the bed level of the right dry cell, $\eta_L > \eta_R = b_R$, the right cell is included in the computational domain. The right face of the dry cell becomes the computational boundary. Temporary adjustment of the bed level and flux in the first cell outside the computation domain as shown in Figure 4 prevents spurious flow in the dry

11

area. In order to increase stability of the model, cells with water depth $d < 10^{-5}$ m are dried automatically. The minuscule amount of water is moved across to a neighbouring wet cell to ensure mass conservation. The above treatment allows for separation of water mass into disjoint blocks with each block of water evolving independently. Such a situation can occur during an overtopping event, where the model can simultaneously calculate the solution in front of as well as behind the overtoppped structure.
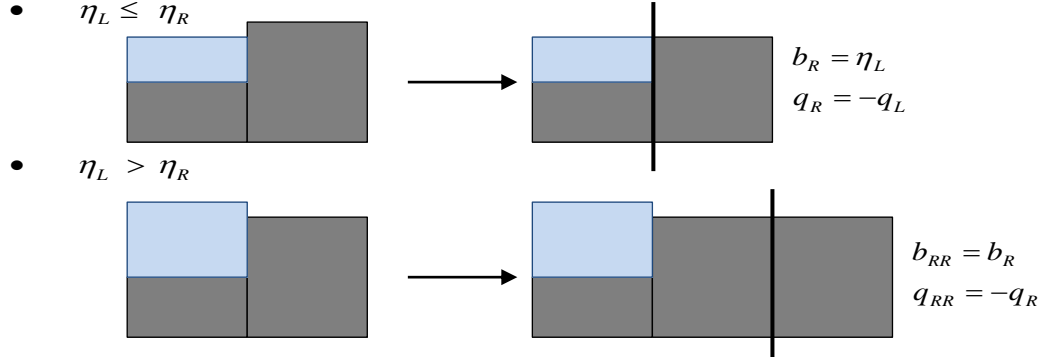

- $\eta_L \leq \eta_R$

$$b_R = \eta_L$$
$$q_R = -q_L$$

- $\eta_L > \eta_R$

$$b_{RR} = b_R$$
$$q_{RR} = -q_R$$

Figure 4: Local bed modification at the wet-dry front according to Brufau et al. (2002).

4. Model verification against analytical solutions

4.1. Exact solitary wave propagation

For flat bottom topography and no bottom friction, the Boussinesq equations by Madsen and Sørensen (1992) in the (ζ, q) formulation are

$$\zeta_t + q_x = 0 \tag{25}$$

and

$$q_t + \left(\frac{q^2}{h + \zeta} \right)_x + g(h + \zeta)\zeta_x = \left(B + \frac{1}{3} \right) h^2 q_{xxt} + Bgh^3 \zeta_{xxx}. \tag{26}$$

For a solitary wave solution, we assume

$$\zeta(x, t) = \zeta(x - Ct) \equiv \zeta(\xi) \qquad \text{and} \qquad q(x, t) = q(x - Ct) \equiv q(\xi), \tag{27}$$

where C is the wave celerity and $\xi = x - Ct$ is the moving ordinate. Further assuming that

$$\lim_{\xi \to \pm\infty} \zeta^{(n)}(\xi) = 0 \qquad \text{and} \qquad \lim_{\xi \to \pm\infty} q^{(n)}(\xi) = 0, \tag{28}$$

the system of equations (25) and (26) reduces to

$$-C\zeta + q = 0 \tag{29}$$

12

and

$$-Cq + \frac{q^2}{h+\zeta} + gh\zeta + \frac{1}{2}g\zeta^2 = -C\Big(B + \frac{1}{3}\Big)h^2 q'' + Bgh^3\zeta'', \tag{30}$$

where the primes denote derivatives with respect to the ordinate ξ. Substituting (29) into (30) we obtain a second order ordinary differential equation for the flux q

$$q''\Big(-C\Big(B + \frac{1}{3}\Big)h^2 + \frac{Bgh^3}{C}\Big) = \Big(\frac{gh - C^2}{C}\Big)q + \Big(\frac{g}{2C^2}\Big)q^2 + \frac{Cq^2}{Ch + q}. \tag{31}$$

Pre-multiplying Equation (31) by q' and integrating with respect to ξ symbolically with Matlab®, we obtain the following first order ordinary differential equation for the flux q

$$\frac{1}{2}(q')^2\Big(-C\Big(B + \frac{1}{3}\Big) + \frac{Bgh}{C}\Big) = -\Big(\frac{C^2}{h}\Big)q + \Big(\frac{g}{2Ch}\Big)q^2 + \Big(\frac{g}{6C^2h^2}\Big)q^3 + C^3\ln\Big(\frac{Ch + q}{Ch}\Big). \tag{32}$$

Setting $q' = 0$ in the above equation provides a relation between the peak flux q_{max} and the wave celerity C. Additionally, using Equation (29) it is also possible to derive a relationship between the solitary wave amplitude A and the wave celerity C such that

$$C = \sqrt{\frac{ghA^2(A + 3h)}{6h^2(A - h\ln(\frac{h+A}{h}))}} = \sqrt{gh\frac{(1 + \frac{1}{3}\frac{A}{h})}{(1 - \frac{2}{3}(\frac{A}{h}) + \frac{2}{4}(\frac{A}{h})^2 - \frac{2}{5}(\frac{A}{h})^3 + \frac{2}{6}(\frac{A}{h})^4 - ...)}}. \tag{33}$$

Therefore for a chosen solitary wave amplitude A and still water depth h, we use Equations (33) and (29) to derive the wave celerity C and the peak flux q_{max} respectively. In order to calculate the flux variation within the wave, Equation (32) with boundary condition $q(0) = q_{max}$ is solved numerically with ode113, an inbuilt ODE solver in Matlab®. The wave profile is then calculated via (29).

A solitary wave of amplitude $A = 0.6$ m propagating in otherwise still water of depth of $h = 1$ m has been calculated using the above method. The result is input as the initial condition for the hybrid numerical model. Figure 5 shows the initial profile (centered at $x = 30$ m) and the subsequent evolution of the solitary wave. The wave propagates without any change of form as expected, confirming that the governing equations have been correctly discretized and accurately time marched. The profiles are deliberately stacked with vertical spacing of 0.6 m to show clearly the non-changing amplitude of the propagating wave. The whole domain is automatically solved by the Boussinesq equations (6), (8) and (9) since the breaking threshold criterion has not been reached.
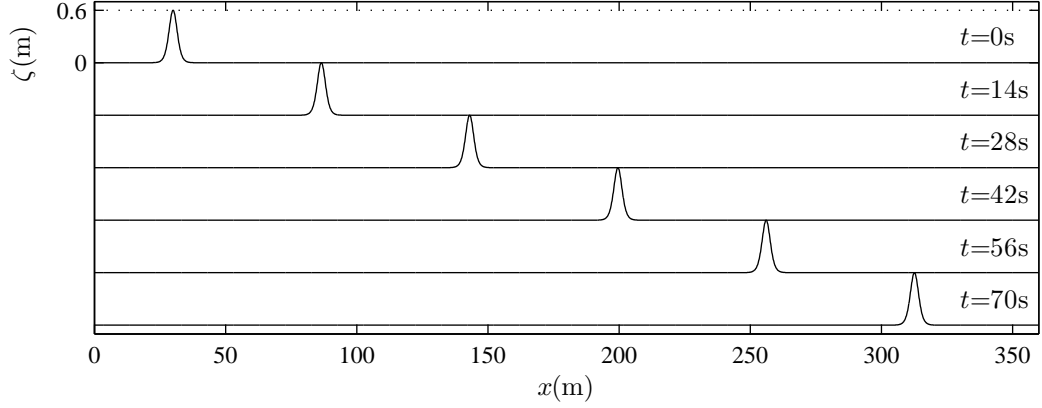
Figure 5: Evolution of the exact $A = 0.6$ m solitary wave.

In this case, the wave celerity to 5 significant figures is $C = 4.0373$ ms^{-1}. Figure 6 shows the numerically predicted and the analytical wave profiles plotted against the moving coordinate $\xi = x - Ct$ at $t = 70$ s. The two profiles coincide, confirming the ability of the numerical model to propagate information at the physically correct speed.
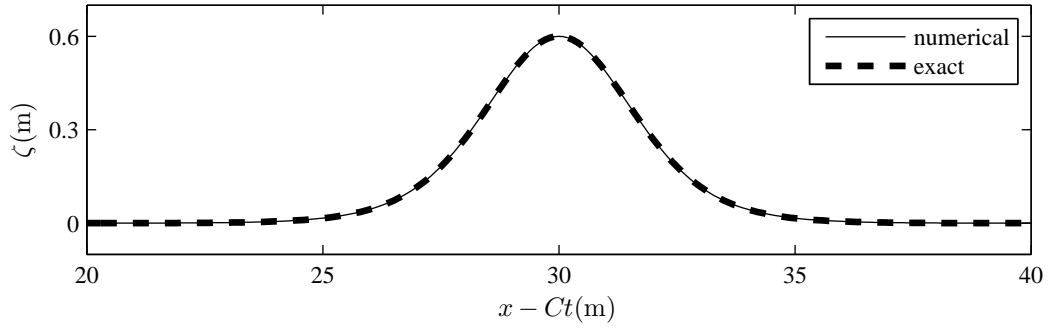

Figure 6: Comparison between the exact and the numerically computed solitary wave plotted against $x - Ct$ at $t = 70$ s.

4.2. Reversibility check

Next, we confirm the reversibility property of the model. A solitary wave of amplitude $A = 0.2$ m is input as the initial condition on otherwise still water of depth of $h = 1$ m. The solitary wave then propagates onto a shelf where the still water depth is reduced to $h = 0.5$ m. The domain configuration is presented in Figure 7.
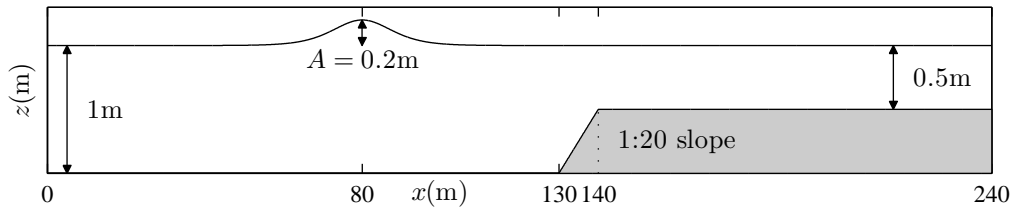

Figure 7: Definition sketch for the submerged shelf reversibility check.

14

The solitary wave propagates unperturbed in the deep water. When it reaches the shelf, it adjusts to the reduced water depth by splitting into several waves. Also, a reflected wave is generated, which travels back from the shelf. Figure 8 shows stacked spatial profiles of the evolving free surface. The grid spacing is $\Delta x = 0.1$ m and the time step is $\Delta t = 0.019$ s.
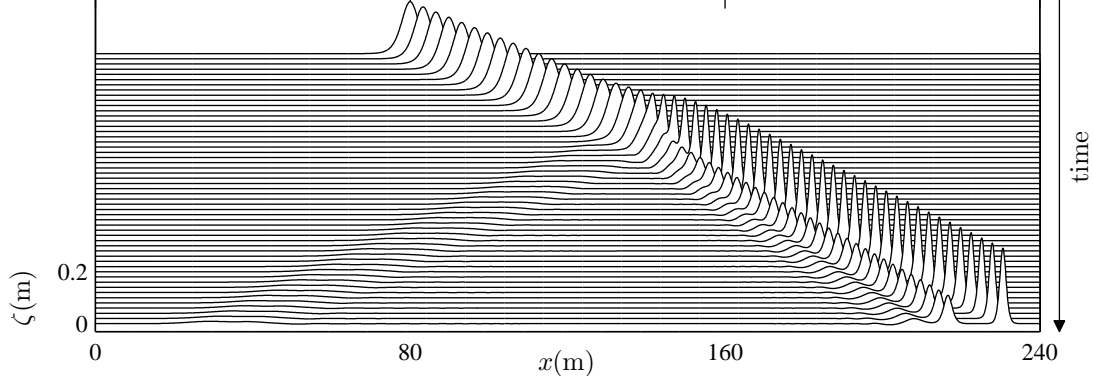
Figure 8: Splitting of a solitary wave. Stacked spatial profiles with time running from the top to bottom.

The final flux and free surface elevation profiles, at $t = 50$ s, are taken as the initial conditions for a reverse simulation, which runs backwards until $t = 0$ s with a negative time step of $\Delta t = -0.019$ s. The shed waves and wiggles, as well as the reflected wave, are absorbed back into the single wave and the original solitary wave is restored, as shown in Figures 9 and Figure 10. We believe this reversibility test to be a very sensitive check on the accuracy of the numerical scheme as it corresponds to a net run time of 100 s and a combined propagation distance of almost 300 m.
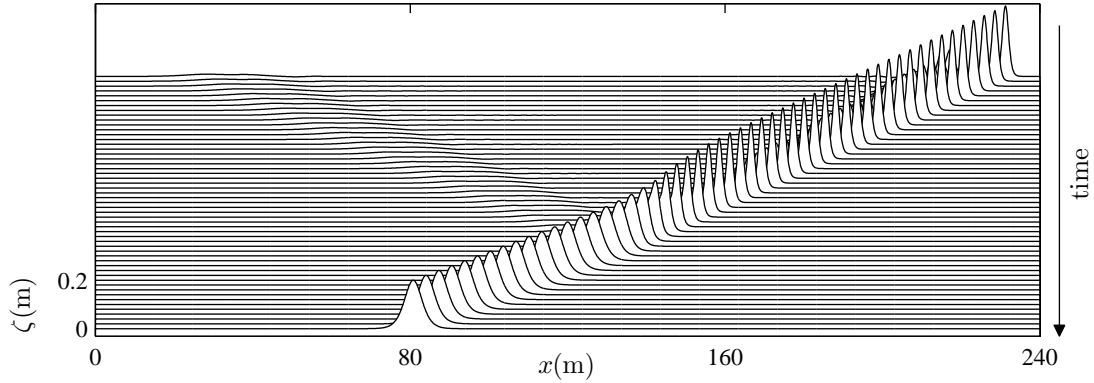
Figure 9: Reverse simulation of a solitary wave splitting. Stacked spatial profiles with time running from the top to bottom.
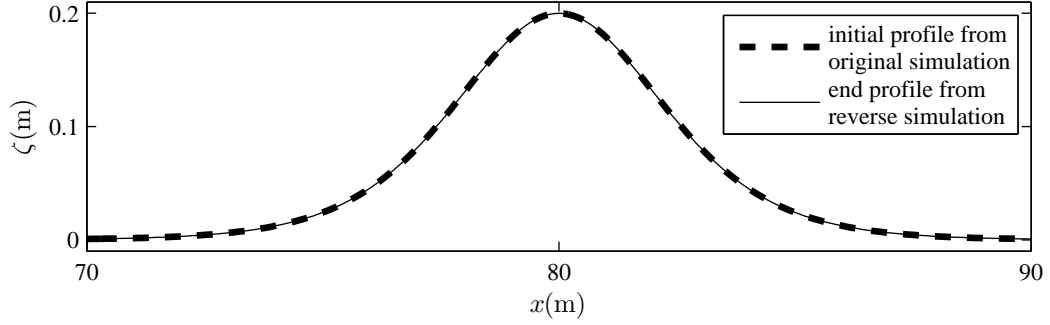
15

Figure 10: Reversibility comparison - end profile of the reversed simulation superimposed on the initial condition of the original simulation.

The reversibility test was additionally used to assess the convergence rate of the model. Here, we have used a sech^2 solitary wave for the initial conditions in order to avoid contaminating the test with hidden errors originating from the ode113 solver. Five different grids were considered, with $\Delta x = 0.8$ m being the coarsest and $\Delta x = 0.05$ m the finest. The corresponding time steps were adjusted accordingly. The errors associated with each grid resolution, expressed in three different norms, were calculated by comparing the end profile from the reverse simulation with the initial profile of the original simulation. The convergence rate is calculated for every grid refinement and is given by the slope, on a loglog plot, of two successive errors plotted against the two corresponding grid resolutions. The model exhibits a roughly fourth order convergence as can be seen from Table 1.

Table 1: Rate of convergence for the sech^2 solitary wave reversibility case.

Δx	$\|\text{error}\|_1$	convergence rate	$\|\text{error}\|_2$	convergence rate	$\|\text{error}\|_\infty$	convergence rate
0.8	1.5078e-1	-	2.9369e-2	-	1.2016e-2	-
0.4	5.7894e-2	1.3810	7.7980e-3	1.9131	2.2762e-3	2.4003
0.2	5.7698e-3	3.3268	5.4819e-4	3.8304	1.1288e-4	4.3338
0.1	3.8624e-4	3.9009	2.5956e-5	4.4005	3.7777e-6	4.9011
0.05	2.4407e-5	3.9841	1.1596e-6	4.4843	1.1934e-7	4.9843

4.3. Wetting and drying algorithm check

In order to validate the wetting and drying treatment in the model, we utilize the analytical solution of the nonlinear shallow water equations for sloshing in a parabolic basin by Sampson et al. (2006). The bottom topography is given by

$$b = \frac{h_0}{a^2}(x - 0.5L)^2, \tag{34}$$

where L is the length of the domain, h_0 is the still water depth at $x = 0.5L$ and a is the width of the basin at elevation $z = h_0$. Following Sampson et al. (2006), for an initial sloping free surface in the wetted region given by

$$\eta(x, 0) = h_0 + \frac{a^2 B^2}{8g^2 h_0}\left(\frac{\tau^2}{4} - s^2\right) - \frac{B^2}{4g} - \frac{Bs}{g}(x - 0.5L), \tag{35}$$

16

the solution for $t > 0$ reads

$$\eta(x,t) = h_0 + \frac{a^2 B^2 e^{-\tau t}}{8g^2 h_0}\left(-s\tau\sin(2st) + \left(\frac{\tau^2}{4} - s^2\right)\cos(2st)\right)$$

$$- \frac{B^2 e^{-\tau t}}{4g} - \frac{e^{-\tau t/2}}{g}\left(Bs\cos(st) + \frac{\tau B}{2}\sin(st)\right)(x - 0.5L), \tag{36}$$

where B, s and τ are constants with $s = 0.5\sqrt{8gh_0/a^2 - \tau^2}$. Sampson et al. (2006) assume linearized friction in the derivation of the above solution, therefore τ satisfies $C_f = \tau\frac{d}{|u|}$.

The computational domain chosen for this validation simulation is 220 m long with resolution of $\Delta x = 1.76$ m. The coefficients are $a = 80$ m, $B = 10$ ms^{-1}, $h_0 = 80$ m and $\tau = 0.1$ s^{-1}. The simulation is run for 80 s with spatial step $\Delta t = 0.04$ s. Figure 11 illustrates the very satisfactory agreement between the analytical solution and the model predictions for the free surface throughout the evolution. The moving shoreline is correctly calculated, validating the wetting and drying algorithm.
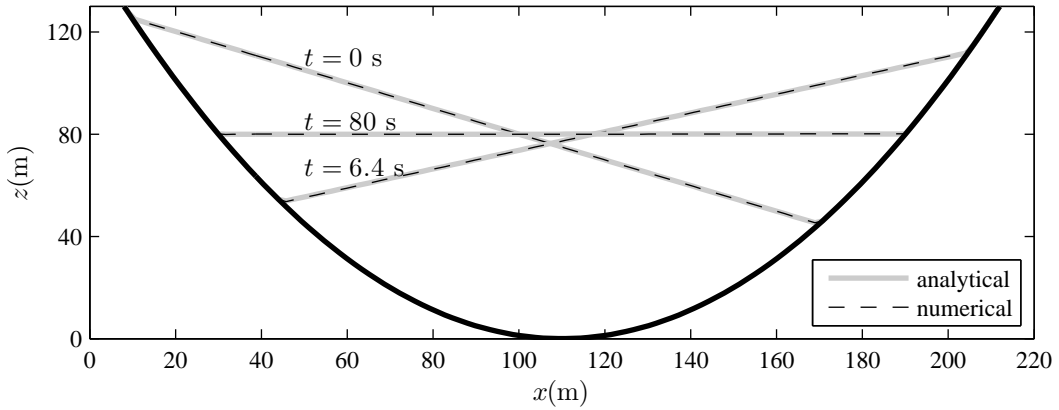

Figure 11: Sloshing in a parabolic basin.

4.4. Paddle wave generation test

The exact solitary wave solution derived in Section 4.1 is used to test the ability of the numerical piston paddle to generate solitary waves of desired amplitude. From Equation (10), to find the desired paddle displacement time series $x_p(t)$, one needs to solve

$$\frac{dx_p}{dt} = \overline{u}(x_p, t) = \overline{u}(x_p - Ct), \tag{37}$$

where $\overline{u} = \frac{q}{\zeta + h}$ with q and ζ being the flux and free surface solitary wave profiles calculated by the method outlined in Section 4.1. Equation (37) is solved forwards and backwards in time from $x_p(0) = 0$ using the ode113 solver in Matlab®. The calculated paddle displacement signal is then fed into the model. Figure 12 shows the generation process for a solitary wave of amplitude $A = 0.6$ m. The correct wave is generated. The profiles are deliberately stacked with vertical spacing of 0.6 m to show clearly the correct amplitude of the generated wave. Also note, that for this case the transition between the *paddle domain* and the rest

of the Boussinesq domain lies at $x = 24.8$ m. From the Figure, it is clear that the solitary wave propagates unaffected as it passes between the two domains, thus confirming correct implementation of non-uniform stencils at grid points $x_{\widetilde{M}-1}$, $x_{\widetilde{M}}$ and $x_{\widetilde{M}+1}$ as described in Section 3.2.
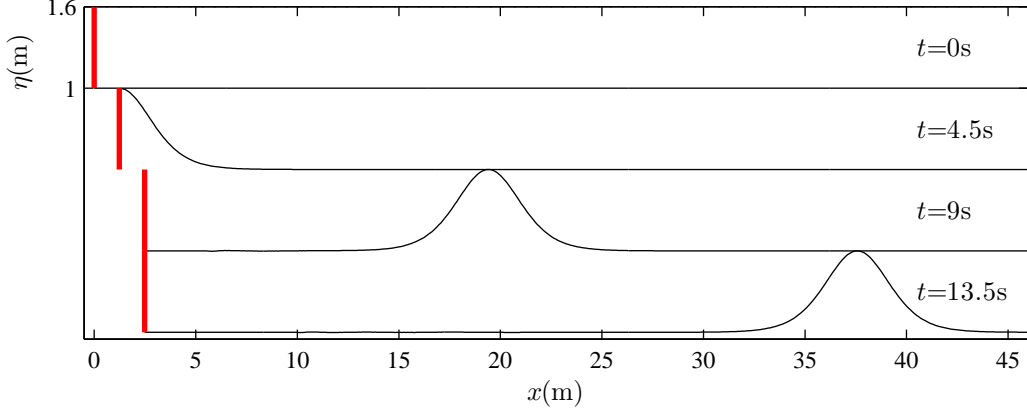

Figure 12: Solitary wave generation using the numerical piston paddle.

Closer examination of the generated wave in Figure 12 reveals very small wiggles trailing the main solitary wave. These could be the consequence of the finite length of the paddle displacement time series or the fact that the solution at the first two grid points adjacent to the paddle is determined from the nonlinear shallow water equations rather than the full Boussinesq equations.

5. Model validation against experimental data

The present model is used to simulate a number of shallow water laboratory experiments. The in-built piston paddle wavemaker is utilised for wave generation. Whenever available, the recorded experimental paddle signals are fed into model. Otherwise, the appropriate paddle displacement time series are calculated using the same methods as were used in the laboratory experiments. Bed friction needs to be chosen for each computational run. For all tests performed in the same experimental facility a consistent friction coefficient is used in the numerical simulations. The UK Coastal Research Facility (UKCRF) and the Tainan supertank basins used comparable materials to construct their laboratory beaches (cement and concrete). The floor in the large-scale supertank basin is relatively smoother, when compared to the water depth and wavelength of the waves generated in the facility. Hence a smaller friction coefficient is used in this case.

5.1. Solitary wave runup at a plane beach

Hsiao et al. (2008) performed a series of experiments on breaking solitary wave runup at a plane beach in the supertank at the Tainan Hydraulics Laboratory, Taiwan. The supertank is 300 m long, 5.2 m deep and 5 m wide. A plane 1:60 beach was constructed 50 m from the wave paddle. Figure 13 shows the layout of the supertank. The free surface elevation was

18

measured by 80 wave gauges. The reference gauge, used for measuring the offshore solitary wave amplitude A, was located at $x = 24$ m. Two offshore (paddle) mean water depths were considered: $h_0 = 1.2$ m and $h_0 = 2.2$ m. Horizontal and vertical runup of the waves were also recorded.
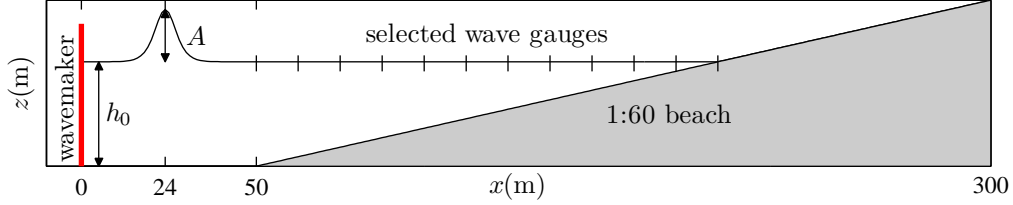

Figure 13: Flume setup for the Tainan supertank experiments reported by Hsiao et al. (2008).

Three experimental runs, covering small to very large solitary wave heights, were reproduced with the present numerical model. Sech^2 solitary waves were generated with the numerical paddle, with the paddle displacement signal calculated according to an algorithm developed by Goring (1978), which was also used by Hsiao et al. (2008) to generate the experimental paddle signals. The friction coefficient was set to $C_f = 0.003$. The computational grid had spatial resolution of $\Delta x = 4$ cm, and the time step was $\Delta t = 0.01$ s. Each simulation was run for 150 s and took about 14 minutes to complete on a standard PC (Intel Xeon 2.93 GHz processor, 6 GB RAM). Figure 14 shows stacked non-dimensionalised free surface time series along the beach; the top series corresponding to the beach toe location and the bottom series to the initial location of the shoreline. The non-dimensionalised variables are indicated by an asterix, and are calculated from $t^* = t/\sqrt{(g/h_0)}$, $\zeta^* = \zeta/h_0$ and $h^* = h/h_0$. From Figure 14 it is obvious that the wave evolution is well predicted by the model. Wave shoaling and breaking, and subsequent bore formation are properly captured. Apart from the maximum crest height being slightly underpredicted, there is very good agreement with the gauge measurements at most locations. For the most nonlinear case, the predicted bore is also slightly larger than measured. Animations of the model's output, synchronised with the measured free surface time series, are available on the web version of this article. Table 2 presents measured and predicted values of the non-dimensionalised vertical runup scaled using $R^* h_0 = R$. There is excellent agreement. The three simulations were repeated on a coarser grid with $\Delta x = 0.08$ m to check that the presented results have converged. The calculated values of the non-dimensional vertical runup were 0.1154, 0.2108 and 0.2598 for the three solitary waves, indicating that a sufficiently refined grid has been used. Numerical simulations of additional runs were carried out and have been reported separately by Orszaghova et al. (2011).

Table 2: Non-dimensionalised vertical runup. Comparison between the model predictions and the Tainan supertank measurements reported by Hsiao et al. (2008).

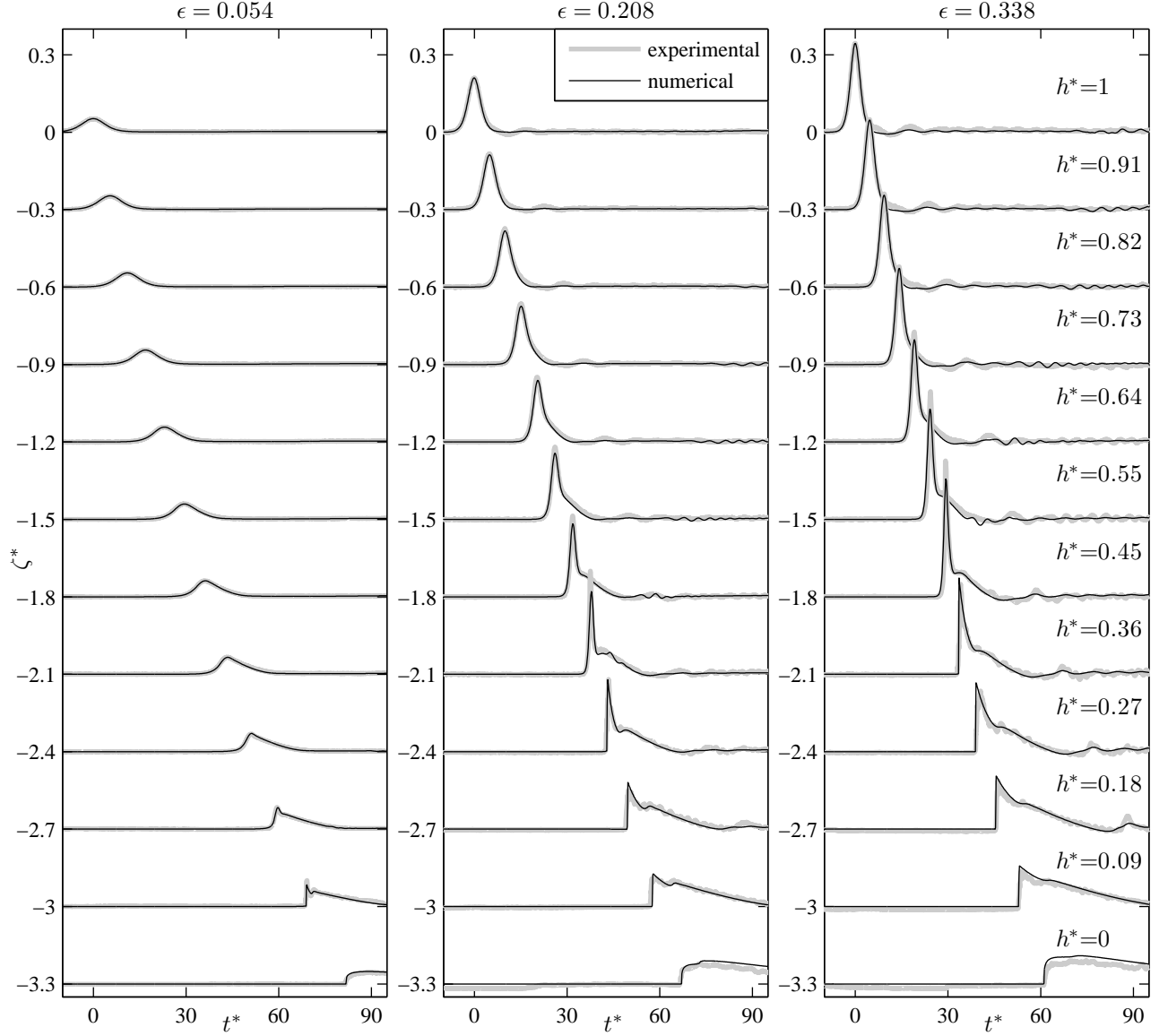| ε	A (m)	h_0 (m)	R^* measured	R^* predicted
0.054	0.119	2.2	0.111	0.1156
0.208	0.249	1.2	0.208	0.2115
0.338	0.406	1.2	0.261	0.2614

Figure 14: Non-dimensionalised free surface stacked time series. Comparison between the model predictions and the measurements from Hsiao et al. (2008).

5.2. Solitary wave overtopping a seawall

Hunt (2003), Hunt-Raby et al. (2011) and Borthwick et al. (2006) report on a large

20

programme of runup and overtopping laboratory experiments in the UK Coastal Research Facility (UKCRF). The basin was 36 m long and 27 m wide, with a segmented piston paddle array for wave generation. A plane 1:20 beach was constructed with its toe located a distance of 8.33 m from the paddles. Additionally, for the overtopping experiments, a laboratory seawall was mounted on the beach at a distance of 8.125 m from the beach toe. The slope of the front face of the seawall was $1 : 2.18$ and the width of the flat top of the seawall was 0.215 m. Free surface elevation was measured by wave gauges placed along the centre line of the basin, including the beach as well as the seawall, if present. Horizontal runup and overtopped volume were also recorded. The basic geometry is shown in Figure 15.
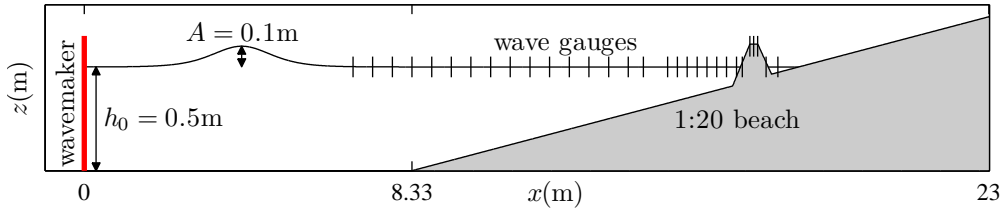

Figure 15: Basin setup for the UKCRF experiments reported by Hunt (2003).

Here we simulate a solitary wave overtopping case with offshore wave amplitude $A = 0.1$ m and offshore mean water depth $h_0 = 0.5$ m, as also depicted in Figure 15. The experiment was replicated with the numerical model on a computational grid of spacing $\Delta x = 1$ cm and time step $\Delta t = 0.0035$ s. The simulation was run for 40 s and took about 6 minutes to complete on a standard PC (Intel Xeon 2.93 GHz processor, 6 GB RAM). The friction coefficient was $C_f = 0.008$ throughout the basin. The sech^2 solitary wave was generated with the numerical paddle using the recorded paddle signal taken directly from the experiment. Figure 16 shows snapshots of the overtopping process. The model correctly captures the wave evolution, including the runup and rundown on the seawall. After overtopping has taken place, the water splits into two blocks, which poses no difficulty to the numerical model. Animation of the entire overtopping event, with superimposed measured data, is available on the web version of this article.
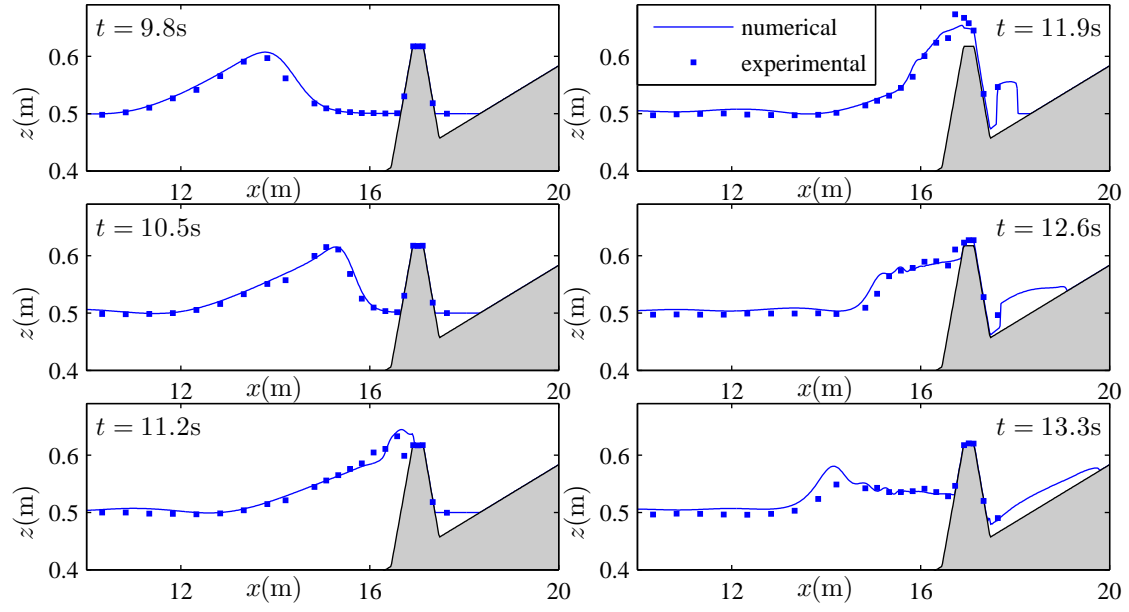
21

Figure 16: Solitary wave overtopping. Comparison between the model prediction and the UKCRF measurements reported by Hunt (2003).
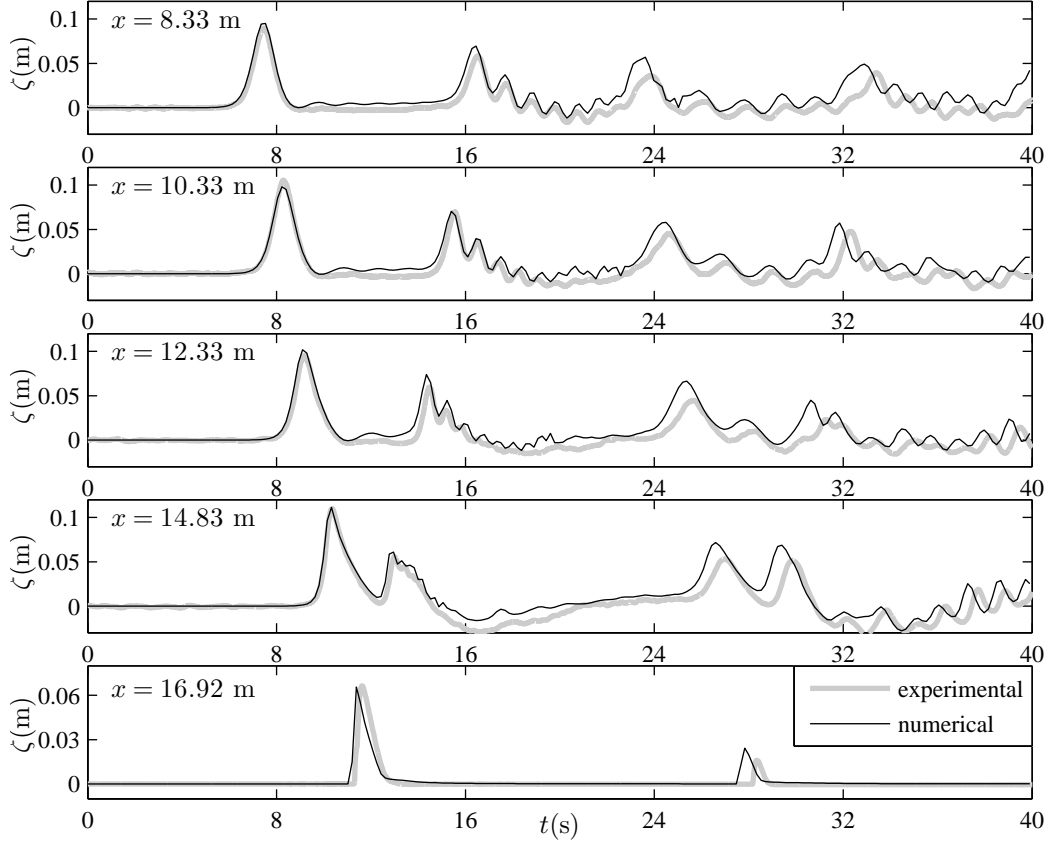
Figure 17: Solitary wave overtopping. Free surface time series comparison between the model prediction and the UKCRF measurements reported by Hunt (2003). Note the vertical scale for the wave gauge on top of the seawall (bottom plot) is magnified.

The overtopped volume per unit length of the seawall was calculated to be 37.51 l/m, whereas the measured volume was 30.6 l/m. The simulation was also repeated on computational grids with spatial resolution of $\Delta x = 0.5$ cm and $\Delta x = 2$ cm (with time steps appropriately adjusted). Overtopped volumes were calculated to be 37.04 l/m and 37.69 l/m, indicating converged results. The present measured and calculated volumes correspond to the total overtopped volume after $40s$, which includes secondary overtopping from the reflected wave. Figure 17 shows free surface time series at five locations along the beach, starting at the beach toe ($x = 8.33$ m) and finishing at the seawall crest ($x = 16.92$ m). The structure of the leading wave is accurately predicted at all locations. However, there is a small but visible difference in the water levels at all initially submerged locations well after the passage of the first solitary wave. It is believed that this is due to volume conservation in the experimental facility, whereby the empty space left behind the paddles as they move forward to generate the solitary wave slowly fills with water from the basin. For a stroke length of around 0.516 m and a still water depth at the paddles of 0.5 m, the displaced volume of water per unit width is roughly 0.25 m^2. Dividing this by the wetted length of the basin (of around 16.5 m) gives a drop of 1.5 cm of the mean water level in the basin after the flow to behind the paddles is complete. This leakage is not accounted for in the model.

23

One could argue that the lower experimental still water levels, after the leak is finished, lead to the mismatch in the secondary overtopping (see Figure 17, location $x = 16.92$ m, $t = 27 - 29$ s) as well as the slight phase difference of the reverberating waves in the basin (see Figure 17, any location, $t > 16$ s). Repeating the simulation with $h_0 = 0.485$ m indeed improves the prediction of the secondary overtopping and the phase of the reflected waves.

5.3. Focused wave group runup and overtopping

The experiments in the UK Coastal Research Facility reported by Hunt (2003), Hunt-Raby et al. (2011) and Borthwick et al. (2006) also included focused wave group runup and overtopping. A focused wave group is composed of individual wave trains that come into phase at one point in time and space to produce a compact energetic event. In a laboratory, focused waves can be generated by appropriately offsetting the longer wave components. In this way, the faster propagating long wave components catch up with the shorter components at the focus location. After focusing, the group disperses with the long wave trains now ahead of the short ones. Using linear theory and for a given underlying wave spectrum, it is straightforward to calculate the paddle displacement signal necessary to generate a focused wave with a desired linear focus location. Applying such a paddle signal pre-multiplied by -1 generates an inverse focused group with troughs, rather than crests, of the wave components coming into phase at the focus location.

Our model is used to replicate a crest- and a trough-focused group each with linear focus amplitude of $A_f = 0.114$ m and linear focus location at 2.5 m up the beach ($x = 10.83$ m). Both the runup on a plane beach and the overtopping of a seawall are presented. The waves are generated using the numerical paddle with the paddle displacement signal recorded from the laboratory experiment. The same friction coefficient of $C_f = 0.008$ was used. The computational grid had spatial resolution of $\Delta x = 1$ cm and the corresponding time step was $\Delta t = 0.0035$ s. Each simulation was run for 90 s and took about 13 minutes to complete on a standard PC (Intel Xeon 2.93 GHz processor, 6 GB RAM).

Figure 18 shows the free surface time series of the crest- and trough-focused wave group overtopping tests. Results are presented from five locations along the beach, starting at the beach toe ($x = 8.33$ m) and finishing at the seawall crest ($x = 17.12$ m). Note that the second location coincides with the linear focus position for the wave groups ($x = 10.83$ m). The model correctly captures wave focusing and steepening as the groups propagate further up the beach. The overtopping flow over the seawall also agrees very satisfactorily with the experimental data, apart from the model failing to pick up additional small overtopping from reflected waves in the crest-focused case at $t = 75 - 77$ s (not shown here). Animations of the overtopping simulations are available on the web version of this article. The predicted and measured overtopped volumes per unit length of the seawall are summarised in Table 3, with maximum difference below 10%. Runup simulations for a 1:20 plane beach (in the absence of the seawall) also gave very satisfactory results. The maximum error in the horizontal runup prediction was below 10%, as can be seen in Table 3. Repeated simulations carried out on computational grids with spatial resolution of $\Delta x = 2$ cm and $\Delta x = 0.5$ cm gave very similar values for the horizontal runup and overtopped volumes (for example crest-focused

wave overtopped volumes were 13.64 l/m and 13.93 l/m respectively) indicating that the presented results are in the asymptotic convergence region.

Table 3: Focused wave group horizontal runup (without the seawall) and overtopped volume per unit length of seawall (with the seawall present). Comparison between the model predictions and the UKCRF measurements reported by Hunt (2003).

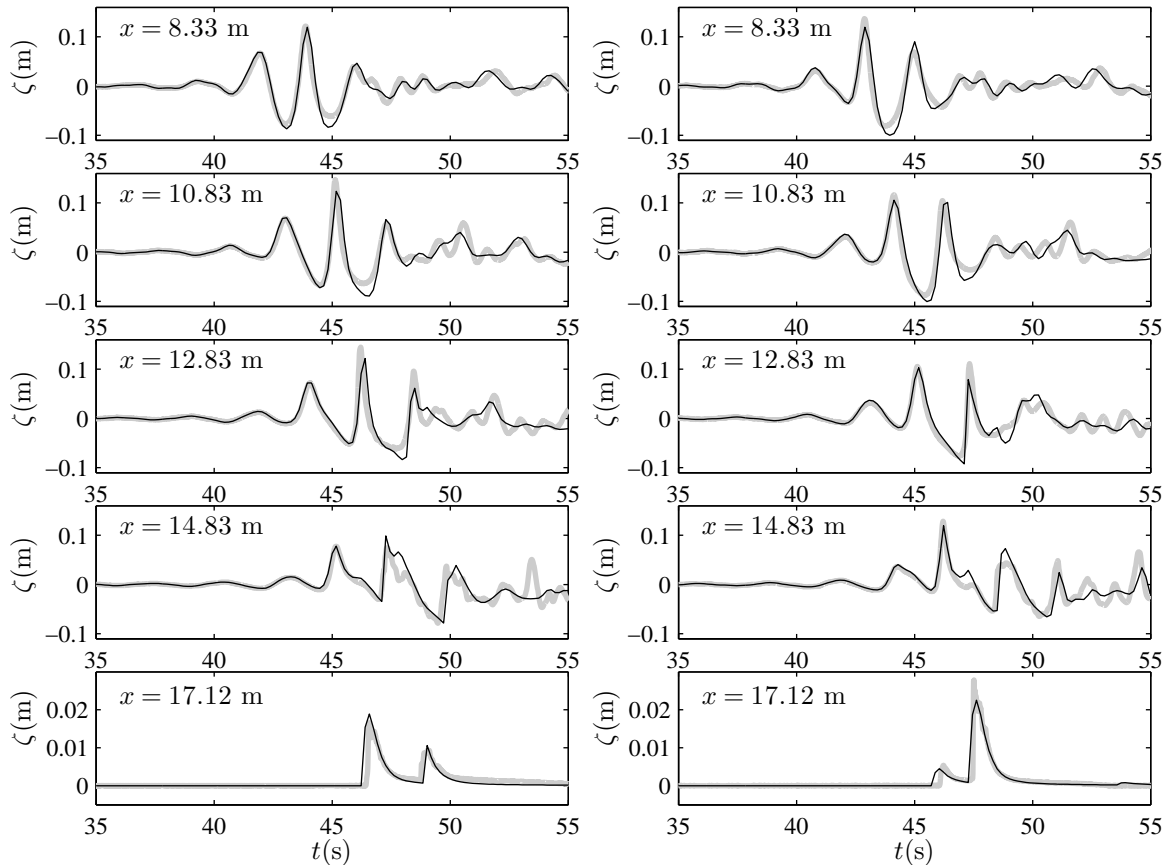| Test	R measured (m)	R predicted (m)	V measured (l/m)	V predicted (l/m)
Crest	2.20	2.41	13.92	14.10
Trough	2.73	2.79	17.29	15.71

Figure 18: Crest- and trough-focused wave group overtopping, with the crest-focused wave shown on the left and the trough-focused wave shown on the right. Free surface time series comparison between the model prediction and the UKCRF measurements reported by Hunt (2003). Thick grey lines represent the measured data. Thin black lines represent the predicted data. Note the vertical scale for the wave gauge on top of the seawall (bottom plot) is magnified.

6. Conclusions

The paper presents a one-dimensional numerical model based on the Boussinesq equations by Madsen and Sørensen (1992) and the nonlinear shallow water equations. The inbuilt

piston paddle acts as a wavemaker in the numerical model, and is incorporated by means of a domain transformation. The numerical paddle has been used successfully to generate a solitary wave, an exact solution of the present Boussinesq equations. It has also been used for complete simulations of a range of shallow water laboratory experiments involving solitary waves and dispersive wave groups, by utilising recorded paddle displacement signals taken directly from the experiments. The model is shown to be suitable for breaking and non-breaking waves. The proposed treatment of breaking, by switching to the nonlinear shallow water equations, works well for all the performed validation tests using a single value of the breaking criterion. This suggests that the breaking treatment and criterion are robust with respect to wave type, without further calibration needed for future tests.

The model has been extensively validated for runup and overtopping scenarios at different physical scales. For solitary waves and compact wave groups, there is very good agreement with measured free surface elevation time series and runup values. Simulations of wave-by-wave overtopping give satisfactory estimates of the free surface elevation at the seawall and overtopped volumes. The numerical wavetank should be useful to engineering practitioners in that the wavetank explicitly incorporates a moving paddle, bed friction, wave breaking and can be used to estimate wave runup and overtopping volumes over sloping seawalls.

The model slightly underestimates wave amplitudes prior to wave breaking, most likely due to the weak nonlinearity assumption of the Boussinesq equations. Future development of the numerical wavetank could include replacing the weakly nonlinear Boussinesq equations with a fully nonlinear version, extension of the model to two horizontal dimensions, incorporation of wave absorption at the paddle and investigating other time integration techniques such as the second order leapfrog method.

Acknowledgements

References

Agnon, Y., Madsen, P. A., Schäffer, H. A., 1999. A new approach to high-order Boussinesq models. Journal of Fluid Mechanics 399, 319–333.

Bellotti, G., Brocchini, M., 2002. On using Boussinesq-type equations near the shoreline: a note of caution. Ocean Engineering 29, 1569 – 1575.

Bonneton, P., Chazel, F., Lannes, D., Marche, F., Tissier, M., 2011. A splitting approach for the fully nonlinear and weakly dispersive Green-Naghdi model. Journal of Computational Physics 230 (4), 1479 – 1498.

Borthwick, A. G. L., Ford, M., Weston, B. P., Taylor, P. H., Stansby, P. K., 2006. Solitary wave transformation, breaking and run-up at a beach. Proceedings of the Institution of Civil Engineers - Maritime Engineering 159, 97 – 105.

Bradford, S. F., Sanders, B. F., 2001. Finite volume schemes for the Boussinesq equations. In: Edge, B. L., Hemsley, J. M. (Eds.), Proceedings of the Fourth International Symposium on Ocean Wave Measurement and Analysis. Vol. 273. ASCE, pp. 953 – 962.

Brufau, P., Vázquez-Cendón, M. E., García-Navarro, P., 2002. A numerical model for the flooding and drying of irregular domains. International Journal for Numerical Methods in Fluids 39, 247 – 275.

Dingemans, M. W., 1997. Water Wave Propagation over Uneven Bottoms, Part 2- Non-linear Wave Propagation. Vol. 13 of Advanced Series on Ocean Engineering. World Scientific, River Edge, NJ.

Fraccarollo, L., Toro, E. F., 1995. Experimental and numerical assessment of the shallow water model for two-dimensional dam-break type problems. Journal of Hydraulic Research 33, 843–864.

Fuhrman, D. R., Madsen, P. A., 2009. Tsunami generation, propagation, and run-up with a high-order boussinesq model. Coastal Engineering 56 (7), 747 – 758.

Gobbi, M. F., Kirby, J. T., Wei, G., 2000. A fully nonlinear Boussinesq model for surface waves. Part 2. Extension to O(kh)4. Journal of Fluid Mechanics 405, 181–210.

Goring, D. G., 1978. Tsunamis- The Propagation of Long Waves Onto a Shelf. Ph.D. thesis, California Institute of Technology, Rep. No. KH-R-38, W.M. Keck Laboratory of Hydraulics and Water Resources, Pasadena, California.

Hsiao, S.-C., Hsu, T.-W., Lin, T.-C., Chang, Y.-H., 2008. On the evolution and run-up of breaking solitary waves on a mild sloping beach. Coastal Engineering 55, 975 – 988.

Hu, K., Mingham, C. G., Causon, D. M., 2000. Numerical simulation of wave overtopping of coastal structures using the non-linear shallow water equations. Coastal Engineering 41 (4), 433 – 465.

Hubbard, M. E., Dodd, N., 2002. A 2D numerical model of wave run-up and overtopping. Coastal Engineering 47, 1 – 26.

Hughes, S. A., 1993. Physical Models and Laboratory Techniques in Coastal Engineering. Vol. 7 of Advanced Series on Ocean Engineering. World Scientific, Singapore ; River Edge, NJ.

Hunt, A. C., 2003. Extreme Waves, Overtopping and Flooding at Sea Defences. Ph.D. thesis, University of Oxford, UK.

Hunt-Raby, A., Borthwick, A. G. L., Stansby, P. K., Taylor, P. H., 2011. Experimental measurement of focused wave group and solitary wave overtopping. Journal Hydraulics Research Accepted.

Johnson, R. S., 1997. A Modern Introduction to the Mathematical Theory of Water Waves. Vol. 19 of Cambridge texts in applied mathematics. Cambridge University Press, Cambridge.

Karambas, T., Koutitas, C., 1992. A breaking wave propagation model based on the Boussinesq equations. Coastal Engineering 18 (1-2), 1 – 19.

Liang, Q., Borthwick, A., 2009. Adaptive quadtree simulation of shallow flows with wet-dry fronts over complex topography. Computers & Fluids 38, 221 – 234.

Lynett, P. J., Melby, J. A., Kim, D.-H., 2010. An application of Boussinesq modeling to Hurricane wave overtopping and inundation. Ocean Engineering 37 (1), 135 – 153.

Madsen, P. A., Bingham, H. B., Schäffer, H. A., 2003. Boussinesq-type formulations for fully nonlinear and extremely dispersive water waves: derivation and analysis. Proceedings of the Royal Society A 459, 1075 – 1104.

Madsen, P. A., Schäffer, H. A., 1999. A review of boussinesq-type equations for surface gravity waves. Advances in Coastal and Ocean Engineering 5, 1–94.

Madsen, P. A., Sørensen, O. R., 1992. A new form of the Boussinesq equations with improved linear dispersion characteristics. Part 2. A slowly-varying bathymetry. Coastal Engineering 18, 183 – 204.

Nwogu, O., 1993. Alternative form of Boussinesq equations for nearshore wave propagation. Journal of Waterway, Port, Coastal, and Ocean Engineering 119, 618–638.

Orszaghova, J., Borthwick, A. G. L., Taylor, P. H., 2011. Boussinesq modelling of solitary wave propagation, breaking, runup and overtopping. Proceedings of the International Conference on Coastal Engineering 1 (32).
URL https://journals.tdl.org/ICCE/article/view/1185

Peregrine, D. H., 1967. Long waves on a beach. Journal of Fluid Mechanics 27, 815–827.

Sampson, J., Easton, A., Singh, M., 2006. Moving boundary shallow water flow above parabolic bottom

topography. In: Stacey, A., Blyth, B., Shepherd, J., Roberts, A. J. (Eds.), Proceedings of the 7th Biennial Engineering Mathematics and Applications Conference, EMAC-2005. Vol. 47 of ANZIAM Journal. pp. 373–387.

Schäffer, H. A., Madsen, P. A., Deigaard, R., 1993. A Boussinesq model for waves breaking in shallow water. Coastal Engineering 20 (3-4), 185 – 202.

Spencer, A. J. M., Parker, D. F., Berry, D. S., England, A. H., Faulkner, T. R., Green, W. A., Holden, J. T., Middleton, D., Rogers, T. G., 1977. Engineering Mathematics, Volume 2. Van Nostrand Reinhold, London.

Stansby, P. K., Zhou, J. G., 1998. Shallow-water flow solver with non-hydrostatic pressure: 2d vertical plane problems. International Journal for Numerical Methods in Fluids 28 (3), 541–563.

Tonelli, M., Petti, M., 2009. Hybrid finite volume - finite difference scheme for 2DH improved Boussinesq equations. Coastal Engineering 56, 609 – 620.

Turnbull, M. S., Borthwick, A. G. L., Eatock Taylor, R., 2003. Numerical wave tank based on a σ-transformed finite element inviscid flow solver. International Journal for Numerical Methods in Fluids 42, 641 – 663.

Wei, G., Kirby, J. T., 1995. Time-dependent numerical code for extended Boussinesq equations. Journal of Waterway, Port, Coastal, and Ocean Engineering 121, 251–261.

Wei, G., Kirby, J. T., Grill, S. T., 1995. A fully nonlinear boussinesq model for surface waves. i. highly nonlinear unsteady waves. J. Fluid Mech 294, 71–92.

Zelt, J. A., 1991. The run-up of nonbreaking and breaking solitary waves. Coastal Engineering 15 (3), 205 – 246.

Zijlema, M., Stelling, G., 2008. Efficient computation of surf zone waves using the nonlinear shallow water equations with non-hydrostatic pressure. Coastal Engineering 55 (10), 780 – 790.